Materials Horizons

ROYAL SOCIETY OF CHEMISTRY

COMMUNICATION

View Article Online
View Journal | View Issue

Cite this: *Mater. Horiz.*, 2024, 11, 480

Received 5th July 2023,
Accepted 6th November 2023

DOI: 10.1039/d3mh01039b

rsc.li/materials-horizons

Room-temperature reversible F-ion batteries based on sulfone electrolytes with a mild anion acceptor additive†

Yifan Yu,[abc] Meng Lei[ac] and Chilin Li *[abc]

Rechargeable fluoride ion batteries (FIBs) as an emerging anion shuttle system are attracting much attention due to their potential advantages in terms of energy density, cost and safety. A liquid electrolyte system enables the FIB operation at low or room temperature due to its higher ionic conductivity than that of a solid F-ion electrolyte. However, the insolubility of fluoride salts in aprotic solvents limits the development of liquid F-ion electrolytes. Although the boron-based anion acceptors (AAs) can facilitate the dissolution of F-ion salts, they are prone to lead to a tough desolvation process for F^- due to strong Lewis acidity and therefore an inferior electrochemical performance. Here, a new non-boron AA (6-thioguanine) with moderate Lewis acidity is proposed to dissolve F^- in the sulfone solvent. The ionic conductivity of the corresponding electrolytes reaches a level of mS cm^{-1} at room temperature. A model FIB coin cell is successfully operated with high conversion reaction reversibility based on the coupled defluorination/fluorination mechanism of electrodes, enabling a low overpotential of 0.36 V and a reversible capacity of 126 mA h g^{-1} after 40 cycles.

New concepts

Multi-electron transfer reactions are of importance to realize high energy density of batteries. In addition to conversion-type cation shuttle batteries, fluoride ion batteries (FIBs) also belong to the conversion reaction battery system based on multi-electron transfer but can cleverly avoid the difficult ion migration caused by strong coulombic interactions between cations and host materials, especially for multivalent cations. However, their limitation is the lack of appropriate electrolytes with mS cm^{-1}-level ionic conductivity at room temperature (RT). One of the significant reasons is that the fluoride salt is insoluble in an aprotic solvent. Boron-based anion acceptors (AAs) facilitate the salt dissociation by the Lewis acid–base interaction between B and F. But this interaction effect also would impede the F^- transport due to the strong Lewis acidity of B, and therefore the conductivity of the corresponding electrolytes is often unsatisfactory (<0.1 mS cm^{-1}). Herein, we report a new AA with mild Lewis acidity, which not only promotes the dissociation of fluoride salt, but also avoids the strong bondage of the AA to F^-. Therefore, the ionic conductivity of the prepared electrolytes can reach up to 2.4 mS cm^{-1} at RT enabling the successful operation of FIBs with a reversible capacity of 126 mA h g^{-1} after 40 cycles. Moreover, the regulation effect of the salt concentration on the cathode interface and then FIB performance is also revealed, suggesting that the rational design of an electrode–electrolyte interface also should be paid attention in the future development of FIBs.

Introduction

In response to the requirements of large-scale energy storage applications,[1,2] various low-cost and high-energy battery chemistries (*e.g.* Li batteries matching with Co-free conversion-type cathodes and multivalent cation and halogen anion batteries) are emerging. Typical conversion-type cathodes (*e.g.* iron fluorides) for Li batteries have the advantages of cost, capacity and energy density when compared with intercalation cathodes containing expensive transition metals.[3–16] However, the usage of Li metal anodes still makes it difficult for a battery system to perform safely and cost effectively under a realistic condition.[17] Multivalent cation batteries (*e.g.* based on Mg^{2+}) also receive much attention in view of their earth-abundant reserves. However a stronger coulombic interaction between these cations and host materials leads to the migration trouble of charge carriers.[18,19] Hence, it is necessary to explore a new shuttle chemistry which enables the cheap and safe implementation of batteries with favorable reaction kinetics and reversibility. Fortunately, recently burgeoning halogen anion batteries could satisfy the above needs.[20,21] Especially for fluoride ion batteries (FIBs), F being the lightest halogen and the most electronegative element endows FIBs with the highest theoretical energy density

[a] State Key Laboratory of High Performance Ceramics and Superfine Microstructure, Shanghai Institute of Ceramics, Chinese Academy of Sciences, 585 He Shuo Road, Shanghai 201899, China. E-mail: chilinli@mail.sic.ac.cn
[b] Center of Materials Science and Optoelectronics Engineering, University of Chinese Academy of Sciences, Beijing 100049, China
[c] CAS Key Laboratory of Materials for Energy Conversion, Shanghai Institute of Ceramics, Chinese Academy of Sciences, Shanghai 201899, China

† Electronic supplementary information (ESI) available. See DOI: https://doi.org/10.1039/d3mh01039b

among the halogen anion batteries, and F^- with the high oxidative stability is beneficial to match with high-voltage electrode materials. Moreover, F as the 13th most abundant element is widely distributed in many continents, and its global production is about two orders of magnitude higher than that of lithium.[22] Conversion-type FIBs (with a theoretical energy density of 5000 W h L^{-1}) even at a leaner stack level can still exhibit an energy density of 588 W h kg^{-1} (1393 W h L^{-1}) but with a cost as low as 20 $ per kW^{-1} h^{-1} according to a techno-economic analysis.[22]

However, such a great merit of energy density for FIBs is not yet realized experimentally and one of the obstacles is the lack of well-tailored electrolytes with suitable ionic transport ability and electrochemical stability. Similar to most cation batteries, FIBs have been developed into two categories based on electrolyte types (*i.e.* solid and liquid electrolytes) since the first experimental proof of rechargeable FIBs reported in 2011.[23] The research of solid-state fluoride ion conductors can be traced back to decades ago or even earlier, but only three main polycrystalline phases with barely satisfactory ionic conductivity were applied in the FIBs, including tysonite, fluorite and tin(II)-based fluorides.[23–27] However, the moderate F^- conductivity of tysonite and fluorite fluorides only allowed the operation of FIBs under high temperature (>100 °C) activation. On the other hand, although the Sn(II)-based fluorides show a relatively high ionic conductivity (10^{-4} S cm^{-1}) even at room temperature,[28] the reactivity of Sn(II) with highly electropositive metal anodes (*e.g.* Li, Ca) and the possibility of oxidation of Sn(II) to Sn(IV) at the cathode side would limit the electrochemical performance of solid-state FIBs.

In this context, liquid electrolytes for FIBs attract the attention of researchers due to their high room-temperature ionic conductivity (up to the mS cm^{-1} level) and better wettability than solid-state electrolytes, which ensure a sufficient contact area between an electrolyte and an electrode. According to the types of fluoride salts, the current liquid electrolytes can be broadly divided into two categories: organic and inorganic fluoride salt electrolytes. The main challenge of liquid electrolytes is the insolubility of fluoride salts in regular organic aprotic solvents, as a result of the strong lattice energy between cations and fluorine ions. Because such a strong electrostatic interaction in fluoride salts leads to the difficulty of F^--solvation, for organic fluoride salts, it is necessary to design a reasonable size and spatial structure of cations to disperse the positive charge and reduce the lattice energy, such as a multi-branched structure.[29] However, such a structure design always involves a complicated synthesis process. For inorganic fluoride salts, firstly, the cations should have low charge density and therefore CsF is a favorable choice because of the large size and low positive charge of Cs^+. Then, anion acceptors (AAs) are indispensable because such additives can contribute to the weakening of Cs^+–F^- interactions *via* the alternative Lewis acid–base (AA-F^-) complexation. Simultaneously AAs can serve as the solvating agents to decrease the Lewis basicity and nucleophilicity of F^-, preventing the potential side reactions between F^- and sufficient acidic atoms from the electrolyte compositions.[22,30] The widely reported AAs are the boron-based compounds, which use the electron-deficient B atoms as the active sites to complex with F^-, thereby improving the solubility of CsF in the ether or siloxane solvent as demonstrated by DFT calculations.[30–33] Despite that these types of electrolytes have realized the cycling of three-electrode FIBs at room temperature, the reversibility is quite undesirable (*i.e.* several to dozens of cycles with severe capacity degradation) accompanied by large voltage polarization. This inferior performance may be due to the excessive solvation of the borides with too strong Lewis acidity. It should be noted that too strong solvation interaction would lead to a tough desolvation process at the electrode/electrolyte interface for F^-, which would participate in the following fluorination reaction of electrodes. Therefore, it is significant to explore new AAs with softer Lewis acidity than borides. Such AAs should not only facilitate the dissolution of fluoride salts to release and solvate F^-, but also make AA-F^- easier to desolvate, in order to develop more practical liquid electrolytes for FIBs.

In this work, we firstly propose a novel sulfone electrolyte based on a new molecular-type H-donor AA (*i.e.* 6-thioguanine, denoted as TG) with moderate Lewis acidity. The TG molecule can serve as the F^- acceptor to interact with F^- *via* the hydrogen atoms on the five-membered ring base, as demonstrated by density functional theory (DFT) calculations and nuclear magnetic resonance (NMR) spectroscopy and Fourier transform infrared (FTIR) spectroscopy. This electrolyte enables an ionic conductivity of 2.40 mS cm^{-1} at room temperature when the salt concentration is 1.0 M. Furthermore, we construct a two-electrode FIB based on this electrolyte (taking CuF_2 and metallic Pb as the cathode and the anode, respectively) and realize its reversible cycling (with a reversible capacity of 126 mA h g^{-1} at 50 mA g^{-1} after 40 cycles) with a polarization voltage of 0.36 V at room temperature. The coupled defluorination and fluorination of CuF_2 and Pb electrodes are confirmed. The superior reversibility of our FIB can be attributed to the high ionic conductivity of the electrolyte, easier desolvation capability of F^- and reasonable interface layer design.

Results and discussion

The preparation process of novel electrolytes and the corresponding optical photographs are illustrated in Fig. 1a and Fig. S1 (ESI†). Firstly, 0.5 M TG was dissolved into colorless and transparent dimethyl sulfoxide (DMSO) and then the color of the solution changed to light yellow. Subsequently, the solution was solidified within minutes upon the addition of 1.5 M fluoride salt (CsF) with a color transition from light yellow to white. This solution was continuously and vigorously stirred overnight to form a white suspension (denoted as CTD3), which was employed as the electrolyte for FIBs. Note that the electrolytes with other concentrations (0.5/1.0/2.0 M) of CsF (denoted as CTD1/2/4, respectively) also display similar experimental phenomena to the above except for the electrolyte without CsF (denoted as CTD0).

To uncover the interaction between TG and CsF, the affinity of TG to F is firstly evaluated by the density functional theory

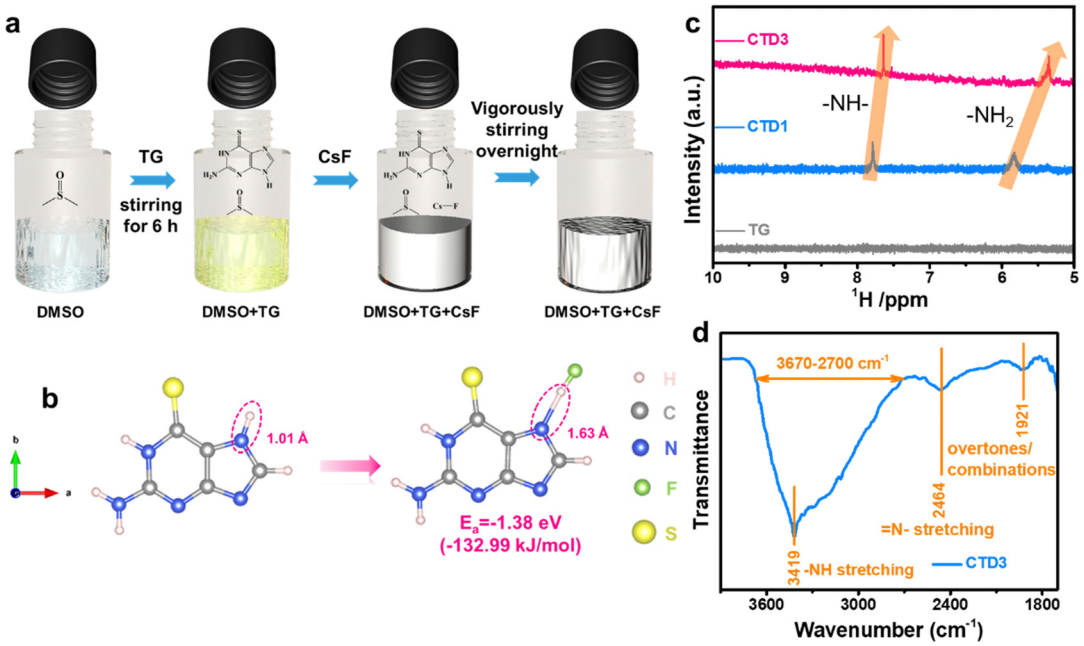

Fig. 1 Preparation and characterization of electrolytes. (a) Preparation process of the CTD3 electrolyte. (b) Illustration of adsorption of the TG molecule to F and its adsorption energy. (c) ^{1}H NMR spectra of TG, CTD1 and CTD3. (d) FT-IR spectrum of CTD3.

(DFT) method as shown in Fig. 1b. The N–H bond from the five-membered ring in TG is elongated after F adsorption and the adsorption energy is −1.38 eV (−132.99 kJ mol^{-1}), lower than that of the reported boron-based AAs (Fig. S2, ESI†). This comparison confirms that TG has moderate Lewis acidity. Nuclear magnetic resonance (NMR) spectroscopy was employed to analyze the underlying interaction involved in the electrolyte. Note that there is no characteristic peak assigned to –NH– or –NH_2 appearing from 10 to 5 ppm in the ^{1}H NMR spectrum for the pure TG sample (Fig. 1c), which may be associated with the selection of a deuterated reagent. After introducing 0.5 M CsF into the electrolyte, two peaks emerge at 7.8 and 5.8 ppm, corresponding to –NH– and –NH_2, respectively.[34] With the increase of the CsF concentration to 1.5 M, the –NH– and –NH_2 peaks exhibit an upfield shift, *i.e.* from 7.8 to 7.6 ppm and from 5.8 to 5.4 ppm, respectively, indicating an electronic effect of CsF on the TG base.[35] In the ^{19}F NMR spectra (Fig. S3, ESI†), the peak signal shows an upfield shift from *ca.* –108 ppm in CsF to *ca.* –113 ppm in CTD1, which suggests an enhanced shielding effect caused by the increased electron density around F. This can be attributed to the formation of a stronger solvation structure of F^- with DMSO and TG in CTD1 than pure CsF in $CDCl_3$. And the peak continues to shift towards the upfield position after further increasing the CsF content, which may result from the electronic effect in view of the increased F^- number around each F^-. Note that there is no obvious change of a chemical shift of peaks in the ^{13}C NMR spectrum (Fig. S4, ESI†), indicating that the electron environment around C from TG is not affected by F^- and C is not the interaction site between TG and F^-. Therefore, combining the calculation results with the NMR experimental results, it is deduced that H from the TG base is the interaction site of TG with F^-. Furthermore, the interaction between TG and F was characterized by Fourier transform infrared (FTIR) spectroscopy. In the FTIR spectrum, a broad band in the region from 3390 to 1750 cm^{-1} is observed for CTD0 (Fig. S5a, ESI†), and it indicates the formation of a TG complex where the TG molecules are chained by hydrogen bonds (Fig. S5b, ESI†). These chains show the large proton polarizability induced by collective proton motion.[36] However, the introduction of CsF induces two significant changes in the FTIR spectrum (Fig. 1d): (1) The narrowing of broad band (from 3670 to 2700 cm^{-1}) reveals the breakage of the hydrogen-bonded chains, which may stem from the interaction between F and the base of TG (Fig. S6, ESI†). This narrowing effect leads to the appearance of some extra bands at low wavenumbers, *e.g.* ═N– stretching at 2464 cm^{-1} and overtones/combinations at 1921 cm^{-1}.[37,38] However, the broad band structure still exists, suggesting that the hydrogen-bonded chains cannot be thoroughly broken by F. (2) The broad band shifts towards the higher wavenumber direction, and the hydrogen bond interaction between F and TG should be responsible for this blue-shift phenomenon.[39]

Fig. 2a shows the ionic conductivity of electrolytes at room temperature. Without CsF, the ionic conductivity is only as small as 6.88 × 10^{-3} mS cm^{-1}. After introducing CsF, the ionic conductivity of the corresponding electrolytes is enhanced by 1000 times, reaching the order of mS cm^{-1}. CTD2 (with a molar ratio of 1 : 2 for TG and CsF) has the highest conductivity of 2.40 mS cm^{-1}, which can be ascribed to the more CsF dissociation. However, the electrolytes of CTD3 and CTD4 with the higher concentrations of CsF display lower ionic conductivity than CTD2. It may be associated with the presence of excessive CsF, which cannot absolutely dissolve. The undissolved CsF as a non-conductive component in the electrolyte likely inhibits the

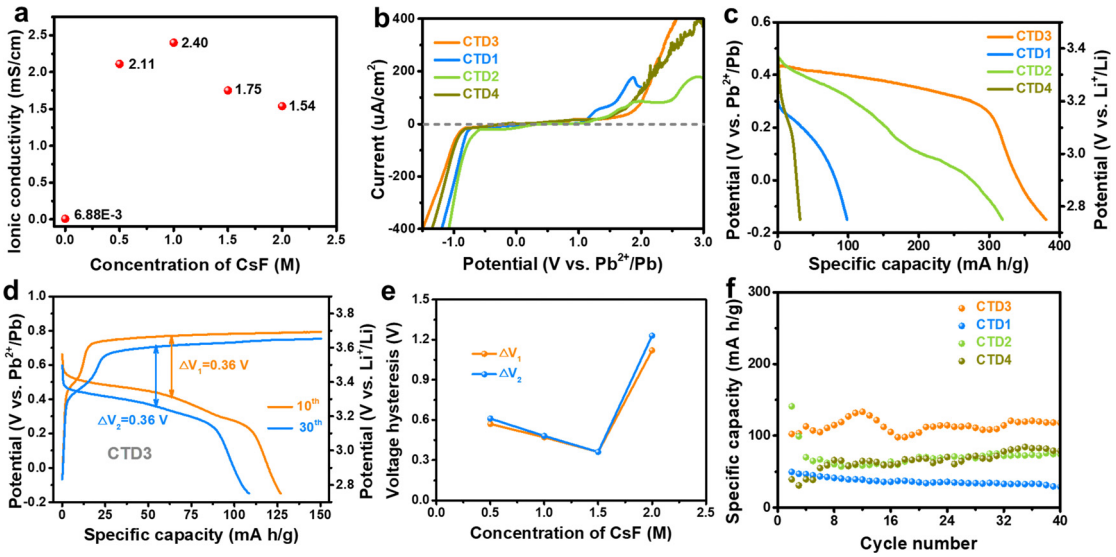

Fig. 2 Electrochemical performance of electrolytes and FIBs at room temperature. (a) Ionic conductivity plots of CTD*n* (*n* = 0,1,2,3,4) electrolytes at room temperature. (b) Linear sweep voltammetry of electrolytes under an architecture of the Al|CTD*n*|Pb cell at a scan rate of 1 mV s^{-1}. (c) Initial discharge curves of CuF_2|CTD*n*|Pb cells. (d) Charge/discharge curves of the CuF_2|CTD3|Pb cell at 50 mA g^{-1} at different cycling stages. (e) Voltage hysteresis of CuF_2|CTD*n*|Pb cells in the 10th and 30th cycles depending on different concentrations of CsF. (f) Cycling performance of CuF_2|CTD*n*|Pb cells from the 2nd cycle.

transport of F^-. In comparison with the reported electrolytes based on boron-based AA molecules, the F^--transport performance of the proposed electrolytes here is at an excellent level (Fig. S7, ESI†). Note that the boron-based AAs that can dissociate and release ions in a solvent by themselves are not discussed here because the released ions may contribute to the potential conductivity (*e.g.* LiBOB *via* the reaction of LiBOB → tLi$^+$ + BOB$^-$).[40] Linear sweep voltammetry (LSV) was adopted to investigate the electrochemical performance of electrolytes in order to determine the voltage range for the subsequent electrochemical measurements. As illustrated in Fig. 2b, CsF can broaden the electrochemical stability of electrolytes likely due to the interaction between CsF and TG. However, the electrolyte with excessive CsF (*e.g.* CTD4) is harmful to the electrochemical performance, which may be related to the side reaction where excessive nucleophilic fluoride attacks some acidic atoms in DMSO or TG.[22] Considering the toxicity and reactivity of elemental fluorine (*i.e.*, F_2) under normal atmosphere and temperature conditions, it is impossible to determine the F^- transport number (t_F) by constructing a F_2–F_2 symmetric cell, as did in the determination of the Li^+ transport number. Therefore, we constructed a symmetric cell using a mixture of Sn and SnF_2 (with a mass ratio of 1 : 1) as electrodes to determine the t_F value based on the Sn + SnF_2|CTD*n*|Sn + SnF_2 configuration with a DC polarization voltage of 10 mV. The t_F value can be obtained according to the following equation:

$$t_F = \frac{I_{SS}(\Delta V - I_0 R_0)}{I_0(\Delta V - I_{SS} R_{ss})}$$

where ΔV is 10 mV, I_0 and I_{ss} are the current responses at the initial and steady states, R_0 and R_{ss} are the corresponding resistances at the initial and steady states. Considering that the only difference among the four electrolytes is the CsF concentration, we measured the t_F values of the electrolytes with the lowest and highest salt concentrations (*i.e.*, CTD1 and CTD4, respectively) as shown in Fig. S8 (ESI†). The $t_{(F,CTD1)}$ and $t_{(F,CTD4)}$ values are estimated to be 0.52 and 0.53, respectively. Obviously, the t_F value remains relatively stable, slightly higher than 0.5, which may be associated with the size of F^- smaller than that of Cs^+. A similar phenomenon has been reported by Davis *et al.*[29] They measured the t_F value using a pulsed-field gradient spin-echo NMR technology and the value was also higher than 0.5.

To validate the applicability of these electrolytes in practical FIBs, a cell with CuF_2 and Pb as the cathode and the anode, respectively, is fabricated. The electrochemical performance of FIBs was evaluated by the galvanostatic discharge/charge method at a current density of 50 mA g^{-1} and under a discharge cut-off voltage of −0.15 V *vs.* Pb^{2+}/Pb and a charge cut-off capacity of 150 mA h g^{-1}. Note that the cut-off charge capacity is set to prevent the potentially undesired side-reactions occurring at the electrode/electrolyte interface. Fig. 2c shows the initial discharge curves of CuF_2|CTD*n*|Pb cells (*n* = 1, 2, 3, 4). The CuF_2|CTD3|Pb cell delivers the highest capacity of 380.5 mA h g^{-1} (equal to 72.0% of the 2e$^-$-transfer theoretical capacity of CuF_2) and shows a discharge plateau of 0.4 V *vs.* Pb^{2+}/Pb. If considering the matching with the Li metal as the anode, the FIB voltage (labeled on the right axis) would be increased to 3.3 V *vs.* Li^+/Li. This plateau can be attributed to the defluorination reaction of CuF_2. The subsequent charge behavior of these cells is shown in Fig. S9 (ESI†). Evidently, the CuF_2|CTD4|Pb cell exhibits the largest voltage polarization in the first cycle and the lowest discharge capacity of 31.8 mA h g^{-1}. The low ionic conductivity and potential side reactions of CTD4 should be responsible for its inferior electrochemical

performance. After dozens of cycles, the discharge curve of the CuF_2|CTD3|Pb cell still exhibits a dominant discharge plateau near 0.4 V *vs.* Pb^{2+}/Pb (Fig. 2d), but the curves of other cells cannot maintain so well (Fig. S10, ESI†). Simultaneously, the CuF_2|CTD3|Pb cell shows the smallest voltage hysteresis of 0.36 V (Fig. 2e), which indicates the best reaction kinetics of the CTD3 based cell. This may be a consequence of the competition between F^--desolvation and ionic conductivity of the electrolyte. Despite that the ionic conductivities of CTD1 and CTD2 are higher than that of CTD3, the CsF concentration in CTD3 is higher and the solvent/TG molecules show a weaker solvation effect on each CsF/F^-, which leads to the easier desolvation of CsF/F^- and participation in the electrode reactions. Moreover, the CuF_2|CTD3|Pb cell can still deliver the highest reversible capacity of 117.6 mA h g^{-1} after 40 cycles at a current density of 50 mA g^{-1} (Fig. 2f). In comparison with other reported FIBs based on liquid electrolytes, the performance of CuF_2|CTD3|Pb is still superior (Fig. S11, ESI†). We also obtained the ^1H and ^{13}C

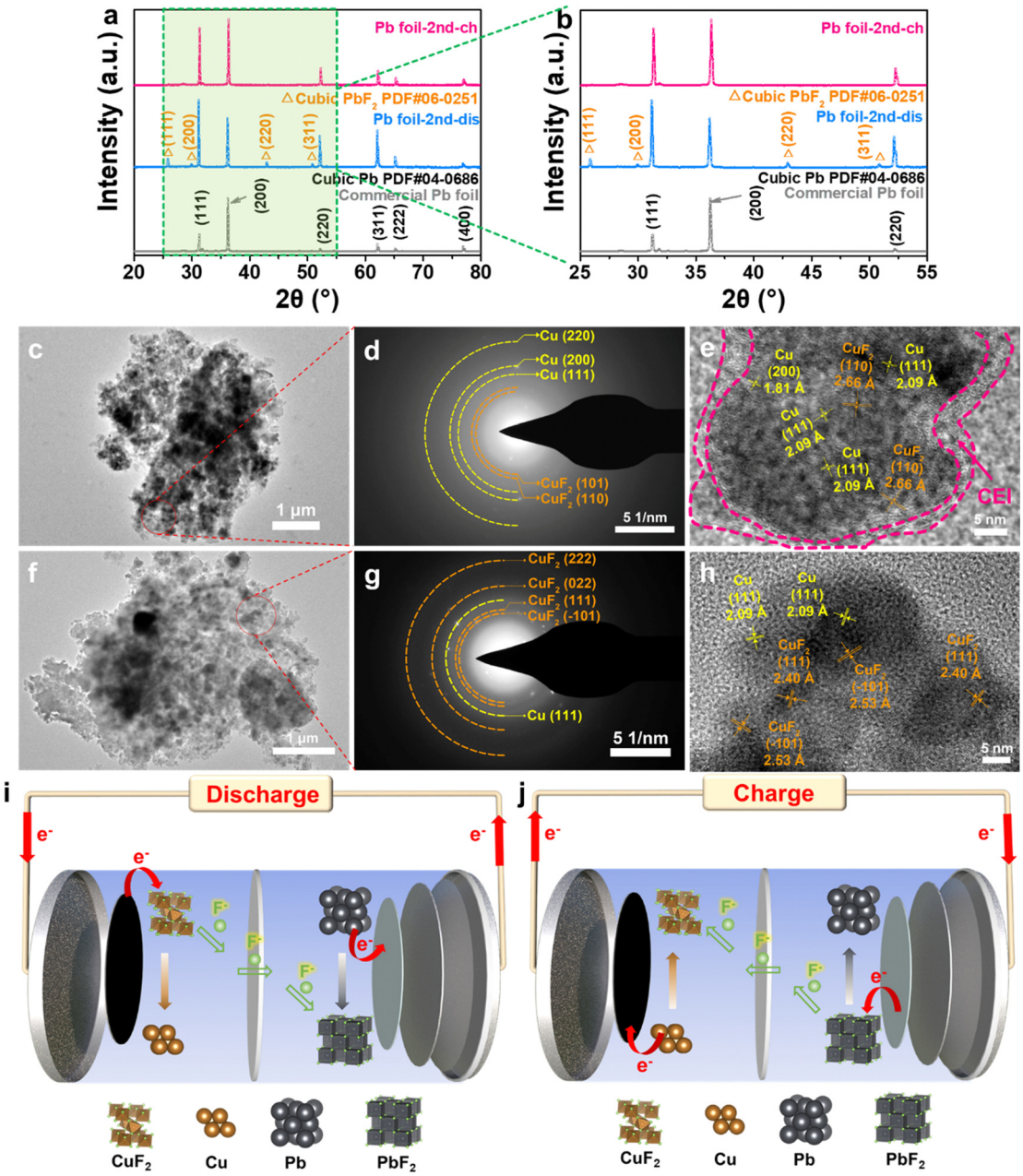

Fig. 3 Structure and phase distribution of cycled electrodes in the CuF_2|CTD1|Pb cell. (a) XRD patterns of cycled Pb anodes. (b) Magnified patterns of the region enclosed by a green dotted rectangle in (a). (c) TEM image of the discharged cathode. (d) SAED pattern of the area enclosed by a red circle in (c). (e) HRTEM image of the defluorinated cathode after discharging. (f) TEM image of the charged cathode. (g) SAED pattern of the area enclosed by a red circle in (f). (h) HRTEM image of the re-fluorinated cathode after charging. Schematic illustration of the conversion reaction mechanism for (i) discharge and (j) charge processes.

NMR spectra of the CTD3 system after 10 cycles. As shown in Fig. S12 (ESI†), the –NH– and $–NH_2$ peaks in the ^1H NMR spectra show a slight downfield shift, *i.e.*, from 7.6 ppm to 7.8 ppm and from 5.4 ppm to 5.5 ppm, respectively. This may be associated with the potential dissolution of cations (Cu^{2+}/Pb^{2+}) in the electrolyte after cycling. The cations can coordinate with F^- and then reduce the interaction between F^- and TG. This effect would reduce the electron density around the H nucleus and result in a slight downfield shift. As for the ^{13}C NMR spectra of electrolytes, there is no obvious change between the pristine CTD3 and CTD3 after 10 cycles. Therefore, the electrolyte can maintain the stability during electrochemical operation and the low coulombic efficiency does not originate from the electrolyte degradation.

The investigation of the coupled defluorination/fluorination reaction in the cathode and the anode is crucial to prove that the operation of conversion-reaction-type FIBs is based on the F^- shuttle. Therefore, the evolution of structures and compositions of the cycled electrodes was investigated. X-ray diffraction (XRD) patterns (Fig. 3a and b) are obtained to analyze the evolution of the crystal structure of the Pb anode. It reveals that the cubic PbF_2 becomes a dominant phase apart from the pristine cubic Pb after discharging, indicating that the Pb anode undergoes a fluorination process during discharging. Subsequently, the diffraction peaks of PbF_2 disappear completely and the cubic Pb becomes the only dominant phase again after charging, which suggests a substantial defluorination process of the anode without the formation of a residue of inactive fluoride. This can be attributed to the F^--conductive nature of PbF_2, which would not block F^- transport and therefore guarantee a highly reversible fluorination/defluorination reaction of the anode.

Moreover, to comprehend the conversion mechanism of the CuF_2 cathode during electrochemical cycling, the morphology and microstructure of the cathode after discharging/charging are studied by transmission electron microscopy (TEM). After the CuF_2|CTD1|Pb cell discharges at −0.15 V *vs.* Pb^{2+}/Pb, numerous fine particles with dark contrast are unevenly distributed in the light-contrast matrix (Fig. 3c and Fig. S13, ESI†). The selected area electron diffraction (SAED) pattern of the selected region marked by a red circle in Fig. 3d confirms Cu^0 as the dominant phase with the formation of an unconverted CuF_2 residue after discharging, which implies an incomplete defluorination process of the CuF_2 cathode. The high-resolution TEM (HRTEM) image (Fig. 3e and Fig. S14, ESI†) further verifies that the fine particles with dark contrast contain some nanodomains surrounded by a thin amorphous layer (named as the cathode electrolyte interface, CEI) with a thickness of 2–3 nm. These nanodomains belong to metallic Cu^0 and residual CuF_2, consistent with the products analyzed from the SAED pattern. The presence of a CEI is beneficial for preventing the cathode from dissolution and preserving the integrity of the powder-type cathode. From the spatial distribution of different domains in the HRTEM image of Fig. 3e, it can be seen that the residual CuF_2 domains are almost surrounded by the Cu^0 domains. Due to the poor F^--ion conductivity of Cu^0, the spatial isolation effect of Cu^0 hinders the leaching of F^- from CuF_2 into the electrolyte and therefore stops the continuous conversion of CuF_2 to Cu^0 (*i.e.* defluorination reaction). This effect is responsible for the formation of a residue of the CuF_2 domains after discharging. After the following charging to 150 mA h g^{-1}, a relatively uniform and dispersed distribution of particles is observed (Fig. 3f and Fig. S15, ESI†). The SAED pattern (Fig. 3g) and HRTEM images (Fig. 3h and Fig. S16, ESI†) all affirm that the dominant phase in these particles is CuF_2, illustrating a re-fluorination reaction from Cu^0 to CuF_2. The retarding effect of fluorination on the mobility of Cu species contributes to the dispersed distribution of particles. The cut-off charge capacity lower than the theoretical capacity of CuF_2 (528 mA h g^{-1} based on $2e^-$ transfer) is the reason for the incomplete fluorination of Cu^0. The presence of residual unconverted Cu^0 may be associated with the inferior F^- transport properties of CuF_2, which prevent the internal Cu^0 from contacting with F^- from the electrolyte and thereby fluorination. According to the XRD results of the Pb anode and TEM analysis of the CuF_2 cathode during electrochemical cycling, the cathode and anode undergo the opposite defluorination/fluorination reactions in the same electrochemical state and the chemical reactions can be written as follows:

$$\text{Discharging process: } CuF_2\ (\text{cathode}) + Pb\ (\text{anode}) \rightarrow Cu + PbF_2 \quad (1)$$

$$\text{Charging process: } Cu\ (\text{cathode}) + PbF_2\ (\text{anode}) \rightarrow CuF_2 + Pb \quad (2)$$

Both the reaction equations intuitively confirm that the operation of this FIB system proposed here is based on a F^--shuttle mechanism (Fig. 3i and j).

As discussed above, the concentration of CsF in the electrolyte seems to exhibit a significant influence on the electrochemical performance of FIBs. Note that the most optimized CsF concentration required for achieving the best electrochemical performance of the cell is not the same as that required for achieving the highest ionic conductivity of the electrolyte. The electrolyte composition has a significant influence on the CEI, which often plays a crucial role in ion transport, maintenance of powder electrode integrity and avoidance of side reactions between the electrode and the electrolyte. Accordingly, it is necessary to conduct comprehensive characterization of the evolution of the CEI chemical composition during electrochemical operation as conducted by X-ray photoelectron spectroscopy (XPS). Note that the CuF_2 cathode was prepared by the ball-milling of commercial CuF_2 and conductive carbon, and the carbon additive would induce the partial reduction of CuF_2 with potential alloying with carbon, which should be responsible for the formation of Cu^0 (568.3 eV in Fig. 4a) and CuC_x (564.7 eV in Fig. 4a and 281.8 eV in Fig. S17a, ESI†) in the pristine cathode.[41] The inevitable introduction of oxygen during ball-milling should account for the appearance of a Cu_2O peak located at 570.1 eV in Cu LMM (Fig. 4a) and 530.7 eV in the O 1s spectra (Fig. S17b, ESI†).[42,43] It seems that Cu_2O does not participate in the reaction, as its peak intensity does not undergo an obvious change during cycling (Fig. S17b and S18b, ESI†).

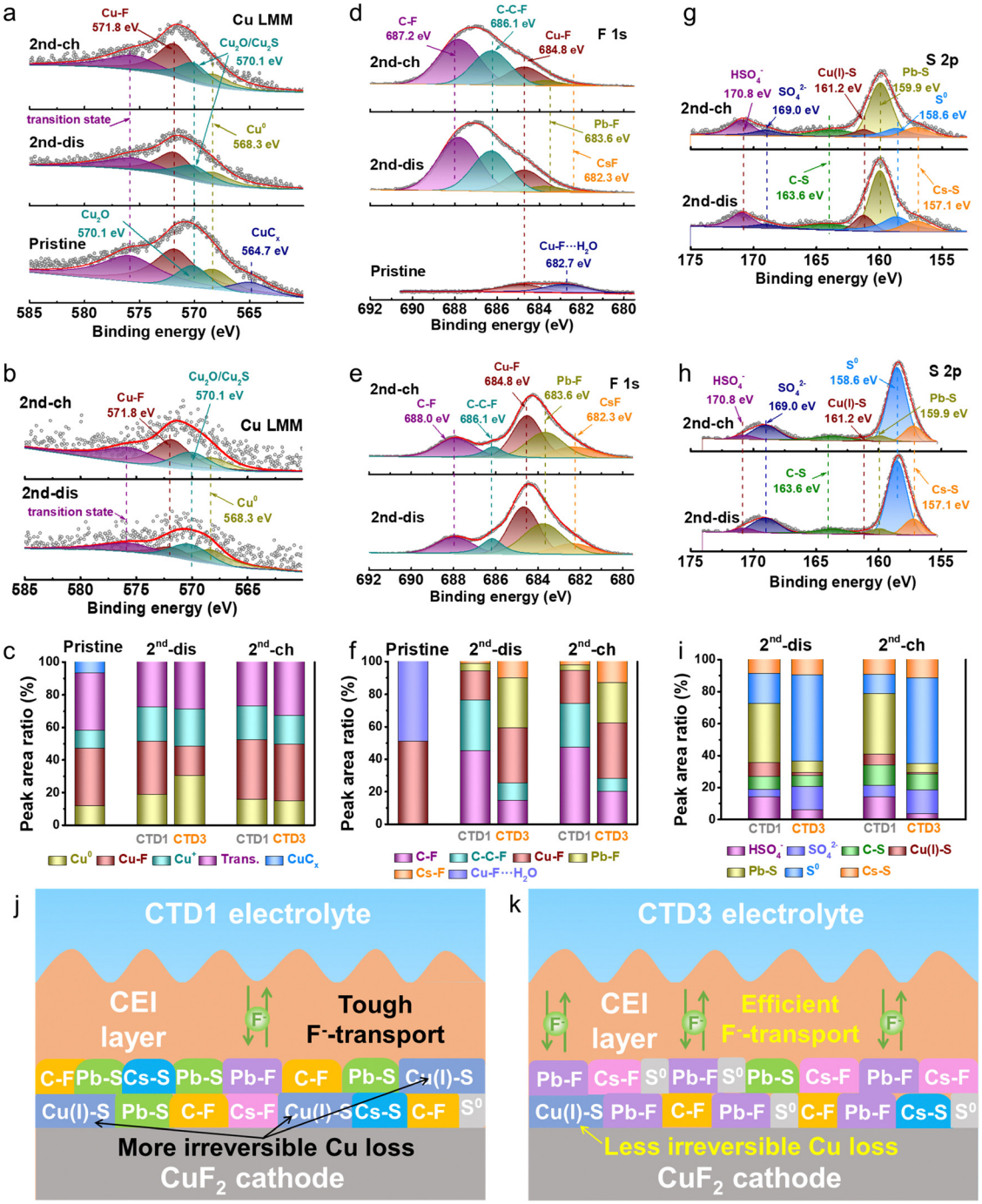

Fig. 4 XPS spectra of pristine and cycled CuF_2 cathodes. (a) Cu LMM, (d) F 1s and (g) S 2p spectra of the pristine cathode and cycled CuF_2 cathode disassembled from the CuF_2|CTD1|Pb cell. (b) Cu LMM, (e) F 1s and (h) S 2p spectra of the cycled CuF_2 cathode disassembled from the CuF_2|CTD3|Pb cell. Peak area ratio of different peaks in (c) Cu LMM, (f) F 1s and (i) S 2p spectra. The "pristine", "CTD1" or "CTD3" denote the pristine cathode, cycled CuF_2 cathode disassembled from the CuF_2|CTD1|Pb or CuF_2|CTD3|Pb cell, respectively. Schematic illustration of the CEI with functional moieties derived from (j) CTD1 and (k) CTD3 electrolytes.

Compared with the pristine state, after discharging at −0.15 V *vs.* Pb^{2+}/Pb, the intensities of peaks in the Cu LMM spectra do not show an obvious change except for the disappearance of the CuC_x signal when CTD1 was used as the electrolyte. However, a significant weakening of intensity of the Cu–F peak at 571.8 eV and a strengthening of intensity of the Cu^0 peak are observed for the CuF_2|CTD3|Pb cell (Fig. 4b).[44] The peak area ratios of the corresponding peaks in the Cu LMM spectra are plotted in Fig. 4c to intuitively reflect the evolution of the relative contents of compositions. Obviously, CuF_2 undergoes a more complete defluorination process in CTD3 than in CTD1 due to the formation of more Cu^0 and a low residue of Cu–F in the

discharged products, which results in a higher discharge capacity of CuF_2|CTD3|Pb. Through the subsequent charging to 150 mA h g^{-1}, Cu^0 is re-fluorinated to CuF_2 and this process is also much more dominant in the CuF_2|CTD3|Pb cell than in CuF_2|CTD1|Pb one. Note that Cu_2S also contributes to the peak at 570.1 eV in the Cu LMM spectra in view of the binding energy of the Cu_2S peak close to that of Cu_2O. The Cu_2S signal may stem from the bonding of the TG derivative with Cu^+ during cycling and it is also validated in the S 2p spectra as discussed later.

As for the F-species in the F 1s spectra, the curve of the pristine state can be deconvoluted into two peaks at 684.8 eV and 682.7 eV (Fig. 4d).[45] The former peak denotes the normal Cu–F bond and the latter one (at lower binding energy) may originate from the formation of a hydrogen bond between F and adsorbed moisture in CuF_2 (Fig. S17b, ESI†). After the electrochemical operation, the peak composition of the spectra becomes more complicated because of the occurrence of potential reactions associated with the CEI formation and electrolyte decomposition. The C–F and C–C–F peaks at 688.0 eV and 686.1 eV, respectively, stem from the binder of poly(vinyl difluoride) (PVDF) as well as the derivative of electrolyte decomposition during the initial cycling (Fig. 4d and e).[46] Recently, a dissolution process of Pb^{2+} was proposed and validated by Okazaki *et al.*, and it is expected to take place before the fluorination of Pb to PbF_2 during discharging.[47] The released Pb^{2+} and and Cs^+ in the electrolyte would combine with F^-, and are responsible for the appearance of Pb–F and CsF peaks at 683.6 eV and 682.3 eV, respectively.[48,49] By comparing the relative peak intensities of different compositions in the F 1s spectra (Fig. 4f), a distinct conclusion can be drawn that CTD3 with a higher CsF concentration benefits the formation of a CEI layer with more Cu–F and Pb–F species and less C–F species (*i.e.* C–F and C–C–F), which indicates the stronger electrochemical stability of CTD3. Considering that PbF_2 is a superionic conductor for F-ions,[50] more Pb–F would promote the F-ion conductivity of the CEI, triggering the efficient and fast F^- leaching (discharging) and supplementing (charging) of the cathode. This effect can reinforce the kinetics of conversion reactions and thereby conspicuously mitigate the voltage polarization even under the condition of lower ionic conductivity of CTD3 than that of CTD1. The CEI optimization further enables a higher discharge capacity release and electrochemical reversibility of FIBs.

The S species in the CEI layer stems from the bonding or complexing between the derivative of TG decomposition and other species (Fig. 4g, h and i). The peaks at 170.8 eV and 169.0 eV belong to HSO_4^- and SO_4^{2-} with the high-valent S element, respectively, and the peak at 163.6 eV should be attributed to the C–S bond.[51,52] Among the low-valent S species, Cu(I)–S, Pb–S and S^0 should be responsible for the peaks at 161.2 eV, 159.9 eV and 158.6 eV, respectively, and the peak at 157.1 eV may be ascribed to the Cs–S bond in view of the low binding energy of the metal–S peak and the presence of a Cs–S bond in the Cs 3d spectra (Fig. S17c and S18c, ESI†).[53–56] By comparing the relative peak intensities of different compositions in the S 2p spectra (Fig. 4i), the S^{2-} species (including Cu(I)–S, Pb–S and Cs–S) in CTD1 are dominant especially the Pb–S moiety, but the dominant species in CTD3 is S^0, suggesting a deeper reduction of TG in CTD1 during cycling. The more negative S^{2-} easily bonds with the cations (*e.g.* Pb^{2+}, Cu^+ and Cs^+), especially the bonding with Pb^{2+} and Cu^+, which would prevent these cations from fluorinating and likely cause the degradation of the F-ion conductivity of the CEI layer and the irreversible loss of the cathode active material. Therefore, the higher CsF concentration in CTD3, on the one hand, can avoid the deeper reduction of the electrolyte, and on the other hand, can provide sufficient F to bond with more cations in competition with S^{2-}. Therefore, it can be validated that the dominant peak for CTD3 is assigned to Cs–F but the strongest peak in CTD1 is assigned to Cs–S in the Cs 3d spectra (Fig. S17c and S18c, ESI†). The weaker C–N and C–S signals in the C 1s and N 1s spectra (Fig. S17d and S18d, ESI†) imply the more robust electrochemical stability of the CTD3 electrolyte, since both the C–N and C–S derive from the TG decomposition.

Briefly, according to the above XPS results, the reason for the better electrochemical performance of FIBs in CTD3 than in CTD1 mainly lies in the higher CsF concentration, which benefits enhancing the electrochemical stability of the electrolyte, enabling the efficient F-ion transport in the CEI layer and mitigating the irreversible loss of cathode active materials (Fig. 4j and k).

Conclusions

In order to develop a practically available liquid electrolyte for FIB operation at room temperature, this work proposes a novel sulfone electrolyte based on a non-boron AA (*i.e.* TG) with softer Lewis acidity than that of boron-based AAs. TG facilitates the dissociation of CsF salt by the interaction between the H atom of –NH on the five-membered ring and F. This electrolyte delivers satisfactory ionic conductivity at a level of mS cm^{-1} at room temperature. A reversible FIB-coin-cell is successfully constructed based on the coupled defluorination/fluorination conversion reaction mechanism of the cathode and anode. The influence of the CsF concentration on the F-ion transport properties of the CEI, mitigation of active material loss, and electrochemical stability of the electrolyte is revealed. The CuF_2|CTD3|Pb cell exhibits the best cycling performance with a reversible capacity of 126 mA h g^{-1} at 50 mA g^{-1} after 40 cycles, benefiting from the suitable ionic conductivity of the electrolyte, an easier desolvation process for F^- and a favorable CEI composition. This work provides new categories of solvents and an anion acceptor additive for liquid electrolytes of FIBs and shows the importance of interface composition in the electrochemical performance of FIBs.

Conflicts of interest

The authors declare no competing interests.

Acknowledgements

This work was supported by the National Natural Science Foundation of China (21975276) and Shanghai Science and

Technology Committee (20520710800). C. Li appreciates the support by the Program of Shanghai Academic Research Leader (21XD1424400).

References

1 J. Baars, T. Domenech, R. Bleischwitz, H. E. Melin and O. Heidrich, *Nat. Sustainability*, 2021, **4**, 71–79.
2 A. W. Schäfer, S. R. H. Barrett, K. Doyme, L. M. Dray, A. R. Gnadt, R. Self, A. O'Sullivan, A. P. Synodinos and A. J. Torija, *Nat. Energy*, 2019, **4**, 160–166.
3 P. L. Lou, C. L. Li, Z. H. Cui and X. X. Guo, *J. Mater. Chem. A*, 2016, **4**, 241–249.
4 P. G. Bruce, S. A. Freunberger, L. J. Hardwick and J.-M. Tarascon, *Nat. Mater.*, 2012, **11**, 19–29.
5 Q. Wu, Z. Yao, X. Zhou, J. Xu, F. Cao and C. Li, *ACS Nano*, 2020, **14**, 3365–3377.
6 R. Li, H. Peng, Q. Wu, X. Zhou, J. He, H. Shen, M. Yang and C. Li, *Angew. Chem., Int. Ed.*, 2020, **59**, 12129–12138.
7 K. Y. Chen, Y. Zhang and C. L. Li, *ACS Nano*, 2018, **12**, 12444–12455.
8 A. W. Xiao, H. J. Lee, I. Capone, A. Robertson, T.-U. Wi, J. Fawdon, S. Wheeler, H.-W. Lee, N. Grobert and M. Pasta, *Nat. Mater.*, 2020, **19**, 644–654.
9 X. Hua, A. S. Eggeman, E. Castillo-Martinez, R. Robert, H. S. Geddes, Z. Lu, C. J. Pickard, W. Meng, K. M. Wiaderek, N. Pereira, G. G. Amatucci, P. A. Midgley, K. W. Chapman, U. Steiner, A. L. Goodwin and C. P. Grey, *Nat. Mater.*, 2021, **20**, 841–850.
10 Q. Huang, K. Turcheniuk, X. Ren, A. Magasinski, A.-Y. Song, Y. Xiao, D. Kim and G. Yushin, *Nat. Mater.*, 2019, **18**, 1343–1349.
11 C. Li, K. Chen, X. Zhou and J. Maier, *npj Comput. Mater.*, 2018, **4**, 22.
12 C. Li, L. Gu, S. Tsukimoto, P. A. van Aken and J. Maier, *Adv. Mater.*, 2010, **22**, 3650–3654.
13 C. Li, C. Yin, L. Gu, R. E. Dinnebier, X. Mu, P. A. van Aken and J. Maier, *J. Am. Chem. Soc.*, 2013, **135**, 11425–11428.
14 K. Chen, M. Lei, Z. Yao, Y. Zheng, J. Hu, C. Lai and C. Li, *Sci. Adv.*, 2021, **7**, eabj1491.
15 K. M. Wiaderek, O. J. Borkiewicz, E. Castillo-Martínez, R. Robert, N. Pereira, G. G. Amatucci, C. P. Grey, P. J. Chupas and K. W. Chapman, *J. Am. Chem. Soc.*, 2013, **135**, 4070–4078.
16 X. Fan, C. Luo, J. Lamb, Y. Zhu, K. Xu and C. Wang, *Nano Lett.*, 2015, **15**, 7650–7656.
17 P. Albertus, S. Babinec, S. Litzelman and A. Newman, *Nat. Energy*, 2018, **3**, 16–21.
18 Z. Yao, Y. Yu, Q. Wu, M. Cui, X. Zhou, J. Liu and C. Li, *Small*, 2021, **17**, 2102168.
19 Z. Yao, Q. Wu, K. Chen, J. Liu and C. Li, *Energy Environ. Sci.*, 2020, **13**, 3149–3163.
20 G. Karkera, M. A. Reddy and M. Fichtner, *J. Power Sources*, 2021, **481**, 228877.
21 M. A. Nowroozi, I. Mohammad, P. Molaiyan, K. Wissel, A. R. Munnangi and O. Clemens, *J. Mater. Chem. A*, 2021, **9**, 5980–6012.
22 A. W. Xiao, G. Galatolo and M. Pasta, *Joule*, 2021, **5**, 2823–2844.
23 M. A. Reddy and M. Fichtner, *J. Mater. Chem.*, 2011, **21**, 17059–17062.
24 H. Bhatia, D. T. Thieu, A. H. Pohl, V. S. K. Chakravadhanula, M. H. Fawey, C. Kübel and M. Fichtner, *ACS Appl. Mater. Interfaces*, 2017, **9**, 23707–23715.
25 Y. Yu, Y. Gu and C. Li, *Energy Storage Sci. Technol.*, 2020, **9**, 217–238.
26 D. T. Zhang, H. Nakano, K. Yamamoto, K. Tanaka, T. Yahara, K. Imai, T. Mori, H. Miki, S. Nakanishi, H. Iba, T. Watanabe, T. Uchiyama, K. Amezawa and Y. Uchimoto, *ACS Appl. Mater. Interfaces*, 2021, **13**, 30198–30204.
27 Y. Yu, M. Lei, D. Li and C. Li, *Adv. Energy Mater.*, 2023, **13**, 2203168.
28 I. Mohammad, R. Witter, M. Fichtner and M. Anji Reddy, *ACS Appl. Energy Mater.*, 2018, **1**, 4766–4775.
29 V. K. Davis, C. M. Bates, K. Omichi, B. M. Savoie, N. Momčilović, Q. Xu, W. J. Wolf, M. A. Webb, K. J. Billings, N. H. Chou, S. Alayoglu, R. K. McKenney, I. M. Darolles, N. G. Nair, A. Hightower, D. Rosenberg, M. Ahmed, C. J. Brooks, T. F. Miller, R. H. Grubbs and S. C. Jones, *Science*, 2018, **362**, 1144–1148.
30 H. Konishi, T. Minato, T. Abe and Z. Ogumi, *J. Electrochem. Soc.*, 2017, **164**, A3702–A3708.
31 A. Celik Kucuk, T. Yamanaka and T. Abe, *J. Mater. Chem. A*, 2020, **8**, 22134–22142.
32 A. Celik Kucuk and T. Abe, *J. Fluorine Chem.*, 2020, **240**, 109672.
33 H. Konishi, T. Minato, T. Abe and Z. Ogumi, *J. Appl. Electrochem.*, 2018, **48**, 1205–1211.
34 J. E. Scott, F. Heatley, D. Moorcroft and A. H. Olavesen, *Biochem. J.*, 1981, **199**, 829.
35 Q. Luo, J. Cao, D. Tang, D. Wu, Y. Huang, J. Xiang, F. Wang, X. Liu and G. Wu, *J. Fluorine Chem.*, 2013, **150**, 67–71.
36 B. Brzezinski and G. Zundel, *J. Mol. Struct.*, 1998, **446**, 199–207.
37 W. Misiuk and M. Zalewska, *Carbohydr. Polym.*, 2009, **77**, 482–488.
38 A. Wesełucha-Birczyńska, C. Paluszkiewicz and B. Borzęcka-Prokop, *J. Mol. Struct.*, 2003, **651–653**, 525–531.
39 X. Li, L. Liu and H. B. Schlegel, *J. Am. Chem. Soc.*, 2002, **124**, 9639–9647.
40 A. Celik Kucuk, T. Minato, T. Yamanaka and T. Abe, *J. Mater. Chem. A*, 2019, **7**, 8559–8567.
41 F. M. Capece, V. D. Castro, C. Furlani, G. Mattogno, C. Fragale, M. Gargano and M. Rossi, *J. Electron Spectrosc. Relat. Phenom.*, 1982, **27**, 119–128.
42 A. Losev, K. Rostov and G. Tyuliev, *Surf. Sci.*, 1989, **213**, 564–579.
43 J. C. Otamiri, S. L. T. Andersson and A. Andersson, *Appl. Catal.*, 1990, **65**, 159–174.
44 G. Johansson, J. Hedman, A. Berndtsson, M. Klasson and R. Nilsson, *J. Electron Spectrosc. Relat. Phenom.*, 1973, **2**, 295–317.
45 R. P. Vasquez, *Surf. Sci. Spectra*, 1993, **2**, 155–159.

46 Y. Hattori, H. Kanoh, F. Okino, H. Touhara, D. Kasuya, M. Yudasaka, S. Iijima and K. Kaneko, *J. Phys. Chem. B*, 2004, **108**, 9614–9618.
47 K.-i Okazaki, H. Nakamoto, T. Yamanaka, T. Fukunaga, Z. Ogumi and T. Abe, *Chem. Mater.*, 2022, **34**, 8280–8288.
48 C. Wagner, W. Riggs, L. Davis, J. Moulder and G. J. E. P. Muilenberg, *Handbook of X-ray photoelectron spectroscopy*, PerkinElmer Corp, Eden Prairie, MN, 1979, p. 38.
49 W. E. Morgan, J. R. Van Wazer and W. J. Stec, *J. Am. Chem. Soc.*, 1973, **95**, 751–755.
50 C. E. Mohn, M. Krynski, W. Kob and N. L. Allan, *Philos. Trans. R. Soc., A*, 2021, **379**, 20190455.
51 N. K. Gupta, J. Bae and K. S. Kim, *New J. Chem.*, 2021, **45**, 22466–22477.
52 J. Yang, X. Zhou, D. Wu, X. Zhao and Z. Zhou, *Adv. Mater.*, 2017, **29**, 1604108.
53 V. G. Bhide, S. Salkalachen, A. C. Rastog, C. N. R. Rao and M. S. Hegde, *J. Phys. D: Appl. Phys.*, 1981, **14**, 1647.
54 X.-R. Yu, F. Liu, Z.-Y. Wang and Y. Chen, *J. Electron Spectrosc. Relat. Phenom.*, 1990, **50**, 159–166.
55 J. Xu, S. Wang, T. Huang, J. Chen and H. Li, *J. Alloys Compd.*, 2022, **929**, 166966.
56 D. Zhao, M. Dai, Y. Zhao, H. Liu, Y. Liu and X. Wu, *Nano Energy*, 2020, **72**, 104715.